POLITECNICO DI TORINO
Repository ISTITUZIONALE

# Growth of metal–organic frameworks on complex copper architectures fabricated by laser powder bed process

*Original*
Growth of metal–organic frameworks on complex copper architectures fabricated by laser powder bed process / Calignano, F., Bove, A., Manfredi, D., Tulliani, J.M.. - In: MATERIALS & DESIGN. - ISSN 0264-1275. - 268:(2026). [10.1016/j.matdes.2026.116618]

*Availability:*
This version is available at: 11583/3013513 since: 2026-07-24T11:05:52Z

*Publisher:*
Elsevier

*Published*
DOI:10.1016/j.matdes.2026.116618

*Terms of use:*

This article is made available under terms and conditions as specified in the corresponding bibliographic description in the repository

*Publisher copyright*

(Article begins on next page)

18 November 2026

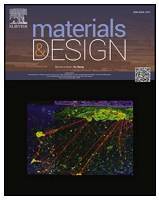
Materials & Design 268 (2026) 116618



Contents lists available at ScienceDirect

Materials & Design

journal homepage: www.elsevier.com/locate/matdes



# Growth of metal–organic frameworks on complex copper architectures fabricated by laser powder bed process

F. Calignano [a,b,*], A. Bove [a,b], D. Manfredi [b,c], J.M. Tulliani [c]

[a] Department of Management and Production Engineering (DIGEP), Politecnico di Torino, Corso Duca degli Abbruzzi 24, 10129 Turin, Italy
[b] Integrated Additive Manufacturing Center (IAM@PoliTo), Politecnico di Torino, Corso Duca Degli Abruzzi, 24, 10129 Turin, Italy
[c] Department of Applied Science and Technology (DISAT), Politecnico di Torino, Corso Duca degli Abbruzzi 24, 10129 Turin, Italy

ARTICLE INFO

*Keywords:*
Additive manufacturing
Laser powder bed fusion process
Pure copper
Metal–organic frameworks
TPMS
Gyroid

ABSTRACT

This study investigated the direct growth of metal–organic frameworks (MOFs) on a copper substrate with complex architecture created via laser powder bed fusion process (PBF-LB/M). Specifically, a scalable route to functionalise gyroid primitive triply periodic minimal surface (TPMS) structures with HKUST-1 ($Cu_3(BTC)_2$, also known as MOF-199) using a malachite-mediated two-step synthesis was analysed. The PBF-LB/M/Cu gyroid architecture provided a high surface-to-volume ratio and favourable curvature for nucleation, enabling uniform formation of $Cu_2(OH)_2CO_3$ nanoribbons across the entire TPMS network. Subsequent conversion into HKUST-1 yielded a continuous MOF coating composed of well-defined octahedral and cuboctahedral crystals. Field emission scanning electron microscopy (FESEM) and computer tomography (CT) scan analysis confirmed homogeneous coverage even in highly curved regions, while X-ray diffraction (XRD) verified the presence of MOF-199 with minimal oxidation of the underlying copper. The lightweight coating (<3 wt%) preserved the openness and thermal conductivity of the metallic scaffold, establishing a robust hybrid platform that bridges metal additive manufacturing with MOF chemistry.

## 1. Introduction

The rapid increase in global energy demand and the continued reliance on fossil fuels are driving a persistent rise in anthropogenic carbon dioxide ($CO_2$) emissions, with a direct impact on global warming and climate change. Mitigation strategies based on energy efficiency are not enough efficient to meet decarbonisation targets such as those outlined in the Paris Agreement. Thus, carbon capture and storage (CCS) and related carbon management technologies have become essential components of any realistic pathway towards substantial $CO_2$ reduction, and adsorption-based separation processes are particularly attractive due to their potential for modularity, low footprint, and integration with existing industrial streams. However, their effectiveness critically depends on the availability of adsorbent materials that combine high capacity, selectivity, and stability under realistic operating conditions [1–5]. Metal–organic frameworks (MOFs) are a class of porous crystalline materials widely used for gas separation [6–8], storage [9–11] and catalysis [12], and are considered a potential solution for applications involving the capture and separation of $CO_2$ [13]. Among the large number of MOFs proposed for $CO_2$ capture, HKUST-1 ($Cu_3$ $(BTC)_2$, also known as MOF-199) has received particular attention [14–18] because it can be synthesised under relatively mild conditions [19,20], exhibits good thermal stability, and offers coordinatively unsaturated copper (Cu) sites that favour $CO_2$ adsorption. Furthermore, its synthesis can be adapted to different morphologies such as powders, films or coatings [4], and the use of copper-based precursors offers opportunities for integrating HKUST-1 with metallic substrates [19]. Despite its excellent $CO_2$ uptake and well-defined pore structure, HKUST-1 is also known to degrade upon exposure to humidity, which has motivated the search for more stable morphologies and synthesis routes [21,22]. The high degree of customisation possible in MOF synthesis has led to the creation of a wide range of MOFs with extremely diverse nano- and microstructural morphologies, which are incorporated into the final macrostructure via 1) coating techniques using MOF-based ink [23,24]; 2) in situ growth of MOFs on the macrostructure [25,26]; 3) incorporation of pre-synthesised nanostructured or microstructured MOFs into the starting material for additive manufacturing (AM)/3D printing [27–29]. AM has been considered as a potential strategy for the fabrication of MOF-based

* Corresponding author at: Department of Management and Production Engineering (DIGEP), Integrated Additive Manufacturing Center (IAM), Politecnico di Torino, Corso Duca degli Abbruzzi 24, 10129 Turin, Italy.
*E-mail address:* flaviana.calignano@polito.it (F. Calignano).

https://doi.org/10.1016/j.matdes.2026.116618
Received 1 June 2026; Received in revised form 3 July 2026; Accepted 16 July 2026
Available online 17 July 2026
0264-1275/© 2026 The Author(s). Published by Elsevier Ltd. This is an open access article under the CC BY-NC-ND license (http://creativecommons.org/licenses/by-nc-nd/4.0/).

**Table 1**
Design parameters for the Cu samples realised as substrate.

| Shape | Cell type | Cell size | Wall thickness | S/V ratio | Relative Density |
|---|---|---|---|---|---|
| Cylinder | Gyroid | 4 mm | 0.3 mm | 10.991 $mm^{-1}$ | 14.59% |

structural and functional devices, where their properties can be controlled by the structural design to suit the practical application. Recently, AM technologies such as material extrusion (MEX), laser beam polymer powder bed fusion (PBF-LB/P), direct ink writing (DIW) and vat photopolymerisation (VAT), have been used to fabricate the customisable MOF components [30–34]. Research has therefore mainly focused on using these AM techniques to construct MOF-enhanced polymer composite components in order to gain advantages in terms of desired shape and geometry, increased surface area and porosity due to the polymer support, and thus improved component performance. The simplest method used in the literature to pattern MOFs using AM is DIW technology, where the MOF is mixed with other chemicals to form a paste that is printed directly [35]. The most complex phase in this technique is in the formulation, which must take into account the accessibility of the MOFs so that they remain porous in the final matrix, as well as the hardness of the object. There are also problems related to the solidification times of the ink. Another possibility is indirect 3D printing, where the MOFs are deposited onto a pre-printed polymer matrix object. This strategy often suffer from limited thermal conductivity, possible incompatibilities between the polymer and the MOF synthesis medium, and long-term stability issues in aggressive environments [36,37]. Recent advances have also introduced MOF-based photopolymerizable inks for high-resolution techniques such as VAT. These inks often incorporate up conversion particle (UCP)-assisted near-infrared photopolymerization (UCAP), which enhances photopolymerization and converts near-infrared light into ultraviolet light to achieve polymerization of photosensitive resins, enabling the precise fabrication of complex MOF structures. [38]. There are studies in the literature that have used the PBF-LB/P for the growth of MOFs [31,39,40]. Despite the advantages of this technology, using the laser can also lead to undesirable results. The study by Li et al. [40] found that MOFs with lower thermostability are more sensitive to process parameters, since when the laser energy settings are too high, MOF crystal decomposition occurs, resulting in carbonization of the top surface of the printed film. This makes it unsuitable to improve the MOF mass loading by increasing the input laser energy.

The direct 3D printing of MOFs is still constrained by the sensitivity of many frameworks to moisture, temperature, and processing solvents, which can lead to degradation or partial loss of crystallinity during shaping [27,36]. A solution can be achieved using the powder bed fusion – laser beam of metals (PBF-LB/M) as an AM process to create architected porous materials based on triply periodic minimal surfaces (TPMS) that are then functionalised with a MOF coating [41], preserving both the mechanical performance of the substrate and the adsorption properties of the framework. TPMS surfaces offer a powerful way to tailor the geometry of the support at the unit-cell level, achieving a high surface-to-volume ratio (S/V), controlled porosity, and interconnected pathways for fluid flow [42,43].

The use of metal substrates produced using AM enables the creation of MOFs on materials with predefined shapes [44,45]. Among the metals used in the PBF-LB/M process, copper is particularly interesting as a MOF support due to its high thermal conductivity, which can mitigate temperature swings during adsorption–desorption cycles, and its electrochemical and catalytic relevance [46,47]. A promising strategy to integrate HKUST-1 with pure copper involves the use of malachite ($Cu_2(OH)_2CO_3$) nanostructures as a first substrate for generating a high surface availability for nucleation points [19]. In this route, a thin layer of malachite is first formed on the copper surface via a mild aqueous treatment and is subsequently converted into HKUST-1 upon exposure to a solution containing the organic linker ($H_3BTC$). Compared with protocols that employ copper nitrates or other soluble metal salts, this approach avoids highly corrosive by-products and improves the overall sustainability of the synthesis [20]. However, combining PBF-LB/M/Cu structures with MOF coatings is far from trivial. First, there is the difficulty of producing the components via PBF-LB/M, given the high reflectivity of copper, which hinders the ability of the metal powder to absorb sufficient laser energy [48]. However, once TPMS structures are successfully fabricated, substrate surface roughness can strongly influence the nucleation of MOFs. While roughness increases surface area for heterogeneous nucleation, it frequently causes poor film morphology, uncontrolled crystal orientations, and pinhole defects that compromise membrane selectivity and electrical contact [49,50]. Another consideration is that the MOF synthesis chemistry must remain compatible with the metal substrate and its surface state.

The purpose of this study was to investigate the growth of HKUST-1 via a malachite-mediated route on copper TPMS structures to verify the continuity of the MOF coating despite the variable surface roughness within the structure resulting from the manufacturing process. The TPMS architecture was designed with a high S/V ratio to maximize the surface area available for MOFs formation while maintaining structural integrity. The copper samples were first post-processed to remove weakly bonded powders and prepare a stable surface for functionalization. The evolution of the surface morphology is investigated at different stages using field emission scanning electron microscopy (FESEM), as well as computer tomography (CT) scan, and the crystalline phases formed are analysed via X-ray diffraction (XRD). Thus, this study wants to demonstrate the feasibility of producing MOF-coated pure copper TPMS structures and provides insight into the interplay between AM surface features, precursor morphology, and final MOF crystal growth. The difficulties related to reach high density values, due to the high reflectivity of copper at the infrared laser sources, are here evaluated as potential aspect for improving the distribution of MOFs on the surface, increasing the available surface for nucleation points. The results highlight the potential of PBF-LB/M/Cu as a functional substrate for MOF-based gas adsorption and separation devices, opening new routes towards architected, thermally conductive adsorbent systems.

## 2. Materials and methods

### 2.1. Samples design and fabrication

The samples were designed using the commercial software nTop (nTop, USA). To achieve a good compromise between sample size and S/V ratio, a trial-and-error approach was followed in designing the samples' TPMS geometry. Different types of cells, cell sizes, and spatial distribution and wall thickness were investigated to find the best S/V. The walled-gyroid structure was infilled with 10 mm diameter and 10 mm height cylinders (Table 1 and Fig. 1).

Gas atomised pure Cu powder provided by EOS GmbH (Germany) was used to built TPMS structures. The particle size distribution (PSD) of the gas atomized powders was determined using a Diffraction Particle Size Analyzer (Mastersizer 3000, Malvern Panalytical). The volumetric PSD was evaluated via analysis of the diffraction angle of a laser when a small amount of powder flows through the chamber, obtaining the following mean values: a D10 of 21 μm, a D50 of 36 μm and D90 of 49 μm. These percentile values indicate that 10%, 50% and 90% of the particles are equal to or smaller than the corresponding size.

A PBF-LB/M machine equipped with a 500 W Yb fibre laser (wavelength at $\lambda = 1060–1080$ nm) and a beam spot size of 100 μm was used to produce PBF-LB/M/Cu test specimens. The steel building platform is heated to 80 °C to improve thermal conductivity and melt the powder layer. The samples were produced in an argon atmosphere to have an oxygen content of less than 0.10%. A silicon blade was used to spread the powder on the platform. Process parameters were chosen that allow

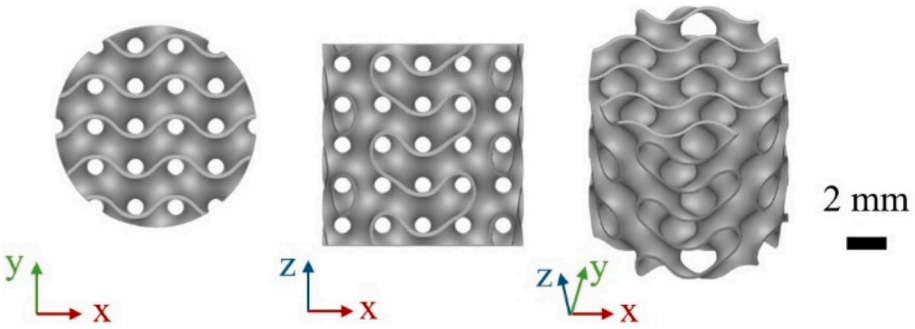



**Fig. 1.** Designed gyroid sample with high S/V ratio.

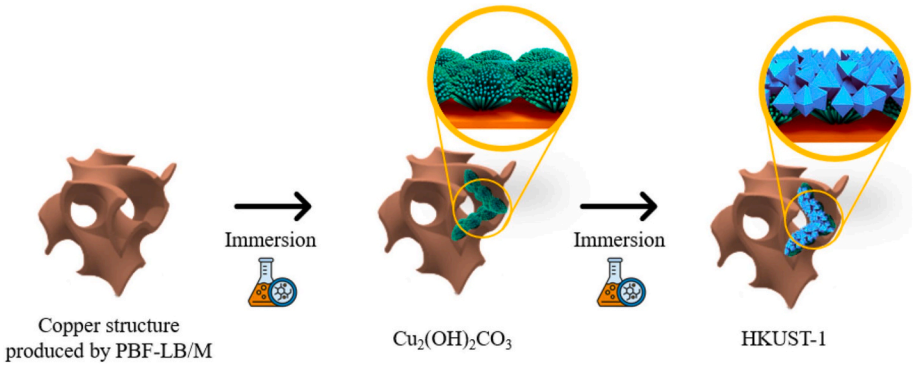



**Fig. 2.** Schematisation of the methodology used: a) construction of the gyroid copper structure in PBF-LB/M; b) preparation of $Cu_2(OH)_2CO_3$ film on pure copper substrate; (c) MOF-199 film on the malachite substrate.

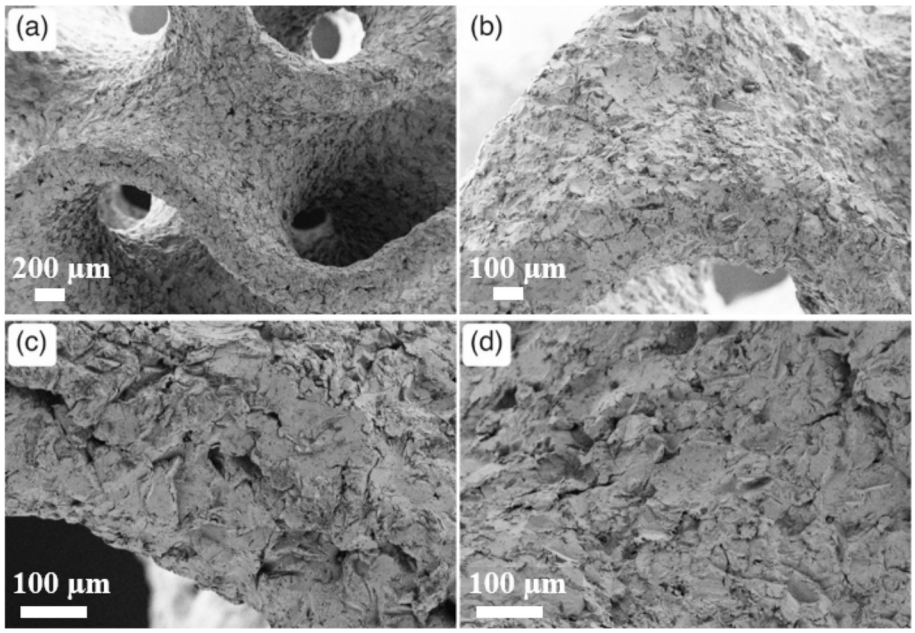



**Fig. 3.** FESEM micrographs of the shot-blast pure copper gyroid sample at different magnifications.

a high density (90%) to give strength to the structure but which at the same time allow for the induction of minimal porosity in the structure which increases the surface area suitable for the growth of MOFs at the same volume: laser power of 370 W, scan speed of 900 mm/s, hatching distance of 0.06 mm and layer thickness of 20 µm [48]. Samples were cleaned after extraction from the build chamber by shot blaster with glass microspheres, which removed unmelted powder particles.

### 2.2. *MOFs growth protocol*

The procedure for substrate surface functionalisation and MOFs growth (Fig. 2) has been realised according to the protocol reported by Du et al. [19].

The printed samples (Fig. 2a) were first sonicated for 10 min in acetone in an ultrasonic bath. Then, an immersion into a solution of 10

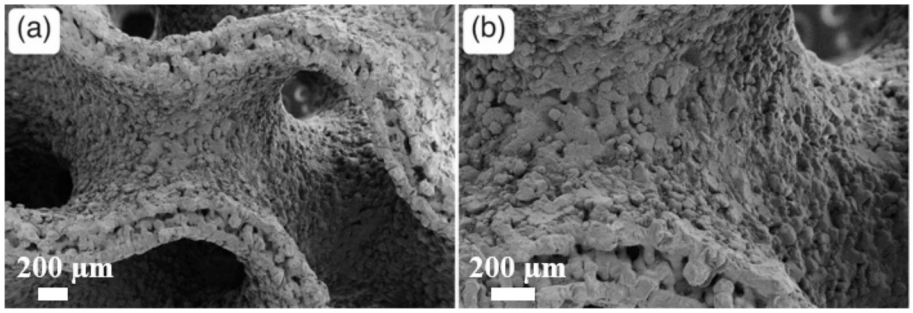



**Fig. 4.** FESEM micrographs of sample 1, with the grown malachite on the functional surface at different magnifications.

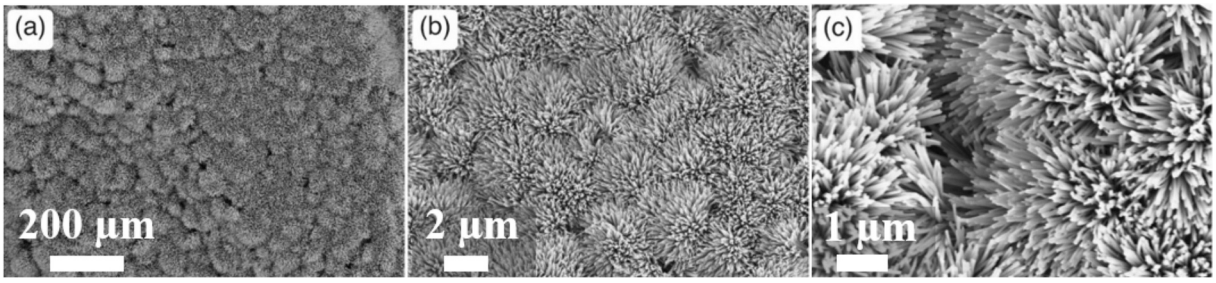



**Fig. 5.** FESEM micrographs of malachite nanoribbons at different magnifications.

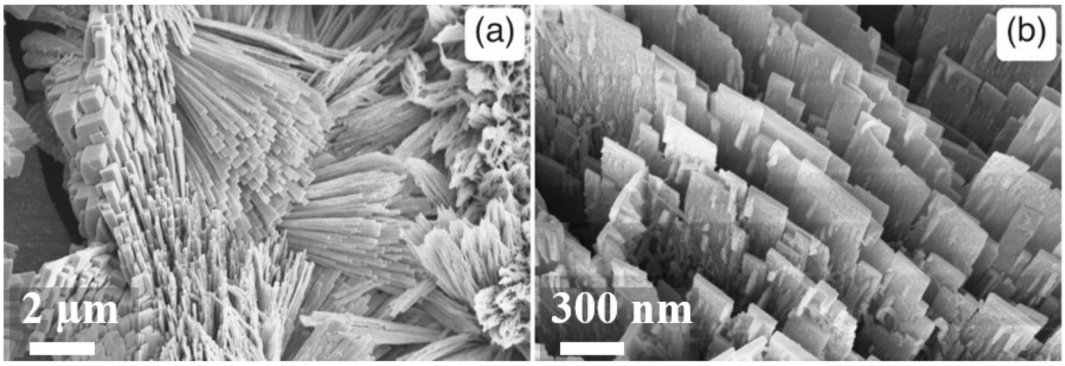



**Fig. 6.** FESEM micrographs of flat and non-homogeneous groups of malachite ribbons at different magnifications.

**Table 2**
Weight changes due to the growing protocol.

| Sample | Cu (g) | Step 1 (g) | Wt% step 1 | Step 2 (g) | Wt% step 2 |
|---|---|---|---|---|---|
| 1 | 1.9876 | 1.9990 | +0.57 | – | – |
| 2 | 1.9499 | 1.9615 | +0.59 | 2.0026 | +2.10 |

mL of sodium bicarbonate ($NaHCO_3$, 1 mol/L), 10 mL of sodium persulfate ($Na_2S_2O_8$, 0.1 mol/L) and 80 mL of distilled $H_2O$ for 24 h at room temperature was performed. The aim of this immersion is to trigger the formation of $Cu_2(OH)_2CO_3$ nanoribbons on the copper surface. The pH of the used solution is about 8. The samples were then rinsed with deionised water and dried in an oven at 60 °C until the achievement of a constant mass (Fig. 2b). One of the treated samples was used for the second step of the protocol, and the growing of HKUST-1 on the functionalised surface was performed. The sample was immersed in a solution made of 18 mL of $H_2O$, 47 mL of ethanol and 0.7 g of 1,3,5-benzenetricarboxylic acid ($H_3BTC$, trimesic acid) for 27 h at room temperature. The resulting pH of this solution is 8.7. A final washing was carried out with water and ethanol, followed by drying in an oven at 60 °C (Fig. 2c).

### 2.3. Characterisations

To control the amount of $Cu_2(OH)_2CO_3$ and HKUST-1 grown on the copper surface, the samples were weighed with an analytical scale KERN ABJ 320-4NM (KERN & SOHN GmbH, Germany). An X-ray diffractometer (XRD, X'Pert Pro, Malvern Panalytical, UK with a Cu anticathode ($\lambda = 0.154056$ nm in the 5-45° 2θ range) was used to collect the relative patterns of the HKUST-1. FESEM (ZEISS, Germany) was used to characterise the morphology of the samples after the two treatments. To evaluate the uniformity of MOF growth, the samples were analyzed using a CT machine (GE *Phoenix* v|tome|x s). The process parameters used for the scans were a voltage of 210 kV, a current of 43 µA, and a voxel size of 9 µm. The analyses were performed using VGStudio Max 3.4 software.

## 3. Results and discussion

### 3.1. Morphology of the copper TPMS substrate

The copper gyroid samples exhibited well-defined TPMS features and a continuous wall surface, confirming the accuracy of the PBF-LB/M/Cu fabrication process. Low-magnification FESEM images (Fig. 3a and 3b)

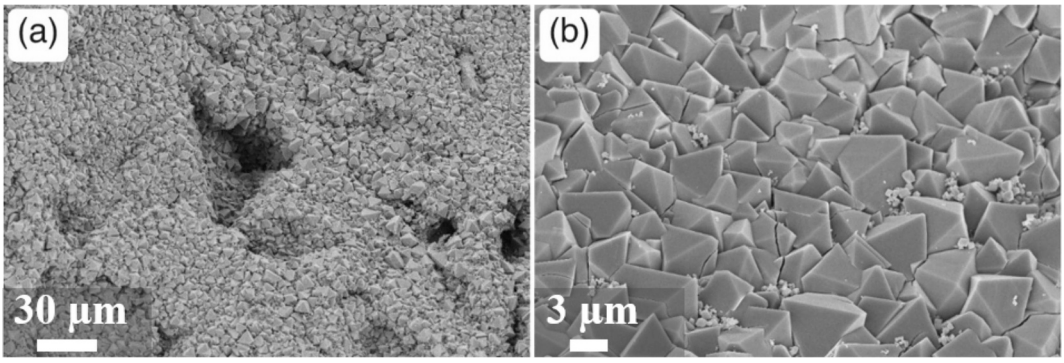



**Fig. 7.** FESEM image of the (a) HKUST-1 layer grown on the $Cu_2(OH)_2CO_3$ substrate, (b) HKUST-1 octahedrons and cuboctahedrons crystals.

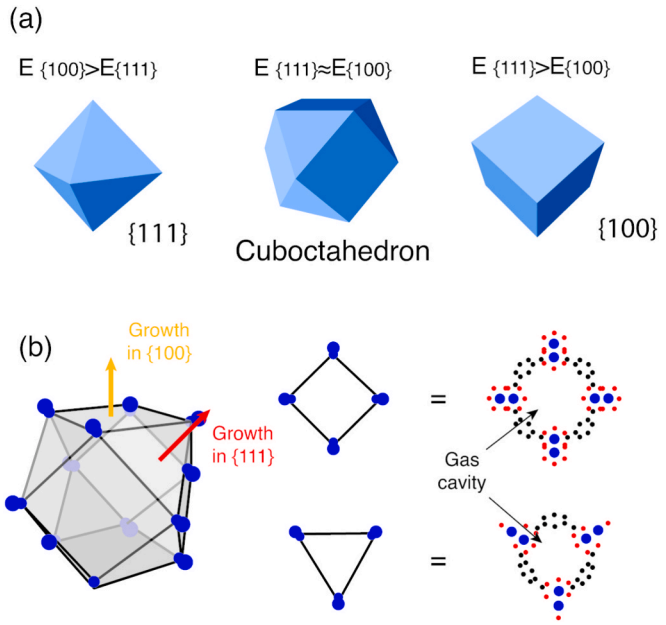



**Fig. 8.** Schematisation of typical growing methods for HKUST-1 crystals; (a) mechanism of cuboctahedron shape formation, (b) $Cu_3(BTC)_2$ is represented by violet spheres, oxygen by red spheres and carbon by black ones. The octahedron is formed by square or triangle windows depending on the superficial energy related to the crystal growth. (For interpretation of the references to colour in this figure legend, the reader is referred to the web version of this article.)

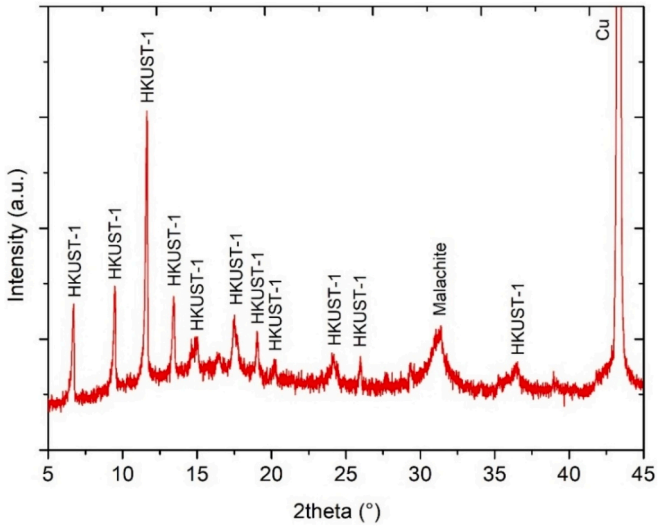



**Fig. 9.** XRD pattern of MOFs crystals grown on sample 2.

show a smooth distribution of the gyroid curvature, with minor interconnected microporosity originating from the chosen process parameters. This controlled microporosity is beneficial for MOF functionalisation, as it increases the number of potential nucleation sites. Higher magnifications (Fig. 3c and 3d) reveal spherical depressions generated by the shot-blaster operation, which effectively removed unfused particles. Surface cleaning provides favourable conditions for homogeneous nucleation in the subsequent malachite growth step. Another relevant observation is the degree of surface oxidation. Local oxide patches appeared on the copper surface, which is expected due to copper's susceptibility to ambient oxidation. While light oxidation does not impede malachite formation, excessive surface oxides can hinder electrical conductivity and introduce local variations in reaction kinetics. Thus, the identified mix of clean copper zones and mildly oxidised areas confirms the importance of the shot-blaster and cleaning sequence prior to chemical functionalization.

**Table 3**
Main peaks and relative intensity of the XRD pattern of the MOFs grown on sample 2.

| No. | 2θ (°) | d-spacing (Å) | Relative intensity (%) | Indexation |
|---|---|---|---|---|
| 1 | 6.71 | 13.17 | 1.46 | HKUST-1 |
| 2 | 9.50 | 9.31 | 1.52 | HKUST-1 |
| 3 | 11.64 | 7.60 | 3.97 | HKUST-1 |
| 4 | 13.43 | 6.59 | 1.14 | HKUST-1 |
| 5 | 14.90 | 5.95 | 0.36 | HKUST-1 |
| 6 | 17.47 | 5.08 | 0.71 | HKUST-1 |
| 7 | 19.05 | 4.66 | 0.64 | HKUST-1 |
| 8 | 20.16 | 4.40 | 0.2 | HKUST-1 |
| 9 | 24.21 | 3.68 | 0.28 | HKUST-1 |
| 10 | 25.97 | 3.43 | 0.38 | HKUST-1 |
| 11 | 31.20 | 2.86 | 0.67 | Malachite |
| 12 | 36.44 | 2.47 | 0.26 | HKUST-1 |
| 13 | 43.31 | 2.09 | 100 | Cu |

### 3.2. *Formation of malachite nanoribbons*

The first chemical step generated a continuous layer of $Cu_2(OH)_2CO_3$ nanoribbons across the TPMS surface. FESEM images (Fig. 4) demonstrate that malachite nucleation is highly efficient on the shot-blaster copper substrate, yielding homogeneous surface coverage even in regions of high curvature.

At higher magnifications (Fig. 5), the nanoribbons appear as radially oriented filiform structures growing from hemispherical centres with

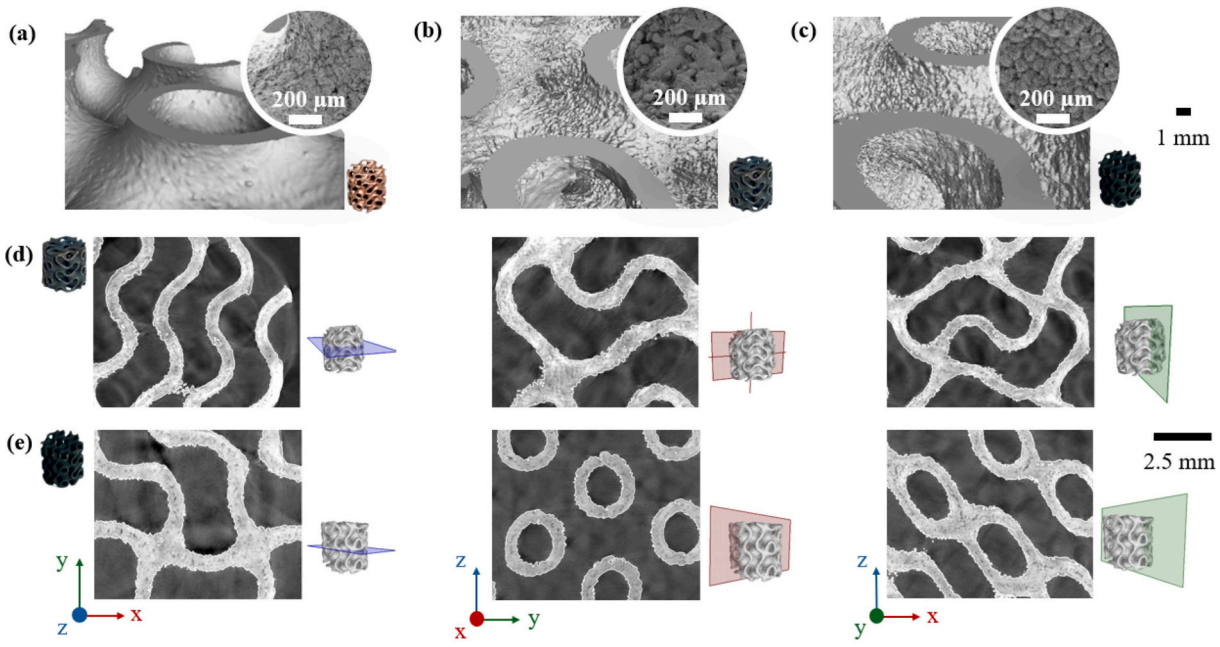



**Fig. 10.** CT scan images: (a) as-built sample; (b) sample with the grown malachite and (c) with the grown HKUST-1 layer; sections along the three principal x, y, and z planes of (d) sample with malachite and (e) sample with MOFs.

radii of approximately 0.5–3 μm. This morphology closely matches previous literature on malachite-mediated HKUST-1 precursors, confirming that the formation mechanism remains effective even on a geometrically complex substrate.

Nevertheless, the malachite layer is not perfectly uniform. Specific regions exhibit larger and less homogeneous aggregates (Fig. 6), characterised by thicker plates or flake-like clusters rather than fine nanoribbons.

These deviations are likely to result from locally reduced nucleation density or surface energy variations. In such areas, slow nucleation favours lateral crystal growth over radial proliferation, leading to non-uniform domains. The overall result is still strongly positive: despite local variations, the malachite layer provides an extensive, reactive, and mechanically well-adhered precursor coating, suitable for conversion into HKUST-1.

### 3.3. Growth and morphology of HKUST-1

Table 2 shows the weight changes due to the two different protocol steps. The growth of MOFs-199 on the $Cu_2(OH)_2CO_3$ substrate was observed via FESEM (Fig. 7). A typical octahedral pyramid structure (Fig. 7b) is exhibited by the MOF-199 crystals, with a fundamental size of ~5 μm.

These findings are comparable to literature [18,35,51,52], confirming the efficiency in the nucleation of MOFs crystals on the malachite nanoribbons generated on additively manufactured pure copper. The crystal shape is typically determined by the coexistence of facets growing with divergent speeds. The octahedron shape is made of eight triangle facets of {111}, which are characterised by a lower superficial energy, making the growth preferential during crystallisation. An intermediate shape can also be formed between the octahedron and the cubic shape when the growing speed of the {100} facets is higher because of a localised superficial energy lower [53]. When the equilibrium energy of {100} is higher than that of {111}, a tetrahedron is formed. When the equilibrium energy of the two geometrical shapes is comparable, cuboctahedrons can be formed. A graphical visualisation is provided in Fig. 8.

The resulting cuboctahedron is thus an intermediate shape which gives to the superficial distribution a heterogeneity that improves the capability of the layer in gas absorption and separation, as reported by Mao et al. [54]. The discrepancies between the geometry are not due specifically to the kinetics of the reaction, but a strong impact of the amount of modulator needs to be considered. By regulating the amount of $H_3BTC$, different crystal shapes and fundamental dimensions can be obtained. When the amount of modulator is high, a preferential growth of octahedron was revealed in literature [19,54]. In Fig. 7b microcracks propagated in the HKUST-1 pattern are evident. These types of cracks are quite typical for MOFs because of their negative coefficient of thermal expansion [55]. This results in a contraction upon heating, which contrasts with the expansion of the substrate, generating an intense stress, triggering microcracking phenomena.

X-ray diffraction analysis confirmed the synthesis of HKUST-1 crystals, and the resulting pattern and relative data are reported in Fig. 9 and Table 3, respectively. The MOFs coating appears to be rather pure: the peaks were attributed to HKUST-1 according to Schlichte et al. [56] and Cu (JCPDF card n° 04–0836). The two small peaks at around 14.5° in 2θ are again characteristics of a hydrated HKUST-1 sample ((331) and (420) reflections) [19]. Neither peaks of CuO (at $2\theta = 35.5°$ and 38.7°, JCPDF card n° 45–0937) nor $Cu_2O$ (at $2\theta = 36.43°$, JCPDF card n° 05–0667) were found in the diffractogram of the synthesised material. The broad peak at about 31.2° in 2θ is probably due to an incomplete reaction of the malachite crystals with BTC; similar results are underlined by Du et al. [19]. The coexistence of the three phases (Cu, malachite, and MOF-199) is confirmed by the XRD pattern analysis, confirming the efficacy of the growing procedure.

Fig. 10 shows the tomography of the sample during the three main phases: creation of the copper structure (Fig. 10a), malachite growth (Fig. 10b), and growth of the MOFs (Fig. 10c). Fig. 10d and 10e show the central and lateral sections with respect to the planes constructed along the Cartesian axes, highlighting the variations in the contours of the gyroid from one stage to the next, demonstrating the uniformity of growth even in the innermost areas of the component.

## 4. Conclusions

This study demonstrates for the first time the feasibility of integrating HKUST-1 coatings with additively manufactured pure copper TPMS architectures through a two-step malachite-mediated route. The

PBF-LB/M/Cu substrate provided a high surface-to-volume ratio and a geometrically complex template capable of supporting uniform formation of $Cu_2(OH)_2CO_3$ nanoribbons, which acted as an efficient precursor for HKUST-1 growth. FESEM observations confirmed homogeneous malachite nucleation across the TPMS walls and successful conversion into HKUST-1 crystals exhibiting both octahedral and cuboctahedral morphologies. While CT scan analysis evidenced the uniformity of MOFs' growth on all the gyroid surfaces. XRD analysis verified the presence of MOF-199 with minimal oxidation of the underlying copper and a minor fraction of unconverted malachite, likely associated with locally dense regions within the precursor layer. Overall, the results highlight that metal additive manufacturing and malachite-based MOF synthesis are highly compatible, even on complex three-dimensional architectures. This approach enables lightweight, mechanically robust, and thermally conductive substrates functionalised with well-defined MOF coatings, opening promising opportunities for architected adsorbent systems, catalytic supports, and thermally managed gas-separation devices.

Other metals will now be investigated, specifically nickel and nickel alloys which potentially allow to grow fluorinated MOFs such as NbOFFIVE-1-Ni (made from $NiNb_2O_5$ and pyrazine ligands) and SIFSIX-3-Ni (built from $NiSiF_6$ and pyrazine ligands) with higher proven $CO_2$ adsorption properties respect to many amine-functionalized MOFs and are more effective for direct air capture of $CO_2$ in realistic environments [57].

## CRediT authorship contribution statement

**F. Calignano:** Writing – original draft, Supervision, Investigation, Conceptualization. **A. Bove:** Writing – original draft, Investigation, Formal analysis. **D. Manfredi:** Writing – original draft, Investigation. **J. M. Tulliani:** Writing – original draft, Supervision, Investigation, Conceptualization.

## Declaration of competing interest

The authors declare that they have no known competing financial interests or personal relationships that could have appeared to influence the work reported in this paper.

## Data availability

No data was used for the research described in the article.

## References


[1] C. Wang, X. Liu, N. Keser Demir, J.P. Chen, K. Li, Applications of water stable metal-organic frameworks, Chem. Soc. Rev. (2016), https://doi.org/10.1039/c6cs00362a.

[2] L. Chen, R. Luque, Y. Li, Controllable design of tunable nanostructures inside metal-organic frameworks, Chem. Soc. Rev. (2017), https://doi.org/10.1039/c6cs00537c.

[3] S. Qiu, M. Xue, G. Zhu, Metal-organic framework membranes: from synthesis to separation application, Chem. Soc. Rev. (2014), https://doi.org/10.1039/c4cs00159a.

[4] T. Ghanbari, F. Abnisa, W.M.A. Wan Daud, A review on production of metal organic frameworks (MOF) for CO2 adsorption, Sci. Total Environ. (2020), https://doi.org/10.1016/j.scitotenv.2019.135090.

[5] A. Hazra, S. Kaskel, Introduction to metal-organic frameworks, Org. Inorg. Mater. Based Sensors (2023), https://doi.org/10.1002/9783527834266.ch2.

[6] H. Li, K. Wang, Y. Sun, C.T. Lollar, J. Li, H.C. Zhou, Recent advances in gas storage and separation using metal–organic frameworks, Mater. Today (2018), https://doi.org/10.1016/j.mattod.2017.07.006.

[7] H. Roohollahi, H. Zeinalzadeh, H. Kazemian, Recent advances in adsorption and separation of methane and carbon dioxide greenhouse gases using metal-organic framework-based composites, Ind. Eng. Chem. Res. (2022), https://doi.org/10.1021/acs.iecr.2c00664.

[8] J.R. Li, R.J. Kuppler, H.C. Zhou, Selective gas adsorption and separation in metal-organic frameworks, Chem. Soc. Rev. (2009), https://doi.org/10.1039/b802426j.

[9] Y.H. Hu, L. Zhang, Hydrogen storage in metal-organic frameworks, Adv. Mater. (2010), https://doi.org/10.1002/adma.200902096.

[10] Y. He, W. Zhou, G. Qian, B. Chen, Methane storage in metal-organic frameworks, Chem. Soc. Rev. (2014), https://doi.org/10.1039/c4cs00032c.

[11] Z. Yang, H. Lu, Q. Li, X. Guo, Q. Li, H. Zhou, B. Wang, Y. Qi, H.C. Chen, M. Yang, T. Tian, H. Yang, J. Ding, H. Pang, Nano/micro metal–organic framework-derived ceramics for sustainable energy saving/capturing, Adv. Mater. (2026), https://doi.org/10.1002/adma.202512289.

[12] Y.S. Wei, M. Zhang, R. Zou, Q. Xu, Metal-organic framework-based catalysts with single metal sites, Chem. Rev. (2020), https://doi.org/10.1021/acs.chemrev.9b00757.

[13] G. Avci, S. Velioglu, S. Keskin, High-throughput screening of MOF adsorbents and membranes for H2 purification and CO2 capture, ACS Appl. Mater. Interfaces (2018), https://doi.org/10.1021/acsami.8b12746.

[14] S.S.Y. Chui, S.M.F. Lo, J.P.H. Charmant, A.G. Orpen, I.D. Williams, A chemically functionalizable nanoporous material [Cu3(TMA)2 (H2O)3](n), Science 80- (1999), https://doi.org/10.1126/science.283.5405.1148.

[15] J. Sun, M. Shang, M. Zhang, S. Yu, Z. Yuan, X. Yi, S. Filatov, J. Zhang, Konjac glucomannan/cellulose nanofibers composite aerogel supported HKUST-1 for CO2 adsorption, Carbohydr. Polym. (2022), https://doi.org/10.1016/j.carbpol.2022.119720.

[16] X. Yan, S. Komarneni, Z. Zhang, Z. Yan, Extremely enhanced CO2 uptake by HKUST-1 metal-organic framework via a simple chemical treatment, Microporous Mesoporous Mater. (2014), https://doi.org/10.1016/j.micromeso.2013.09.009.

[17] A.R. Millward, O.M. Yaghi, Metal-organic frameworks with exceptionally high capacity for storage of carbon dioxide at room temperature, J. Am. Chem. Soc. (2005), https://doi.org/10.1021/ja0570032.

[18] A. Bertero, J. Schmitt, H. Kaper, B. Coppola, P. Palmero, J.M. Tulliani, MOFs functionalization of 3D printed mullite complex architectures for CO2 capture, Appl. Mater. Today (2024), https://doi.org/10.1016/j.apmt.2024.102407.

[19] J. Du, C. Zhou, Z. Yang, J. Cheng, Y. Shen, X. Zeng, L. Tan, L. Dong, Conversion of solid Cu 2 (OH) 2 CO 3 into HKUST-1 metal-organic frameworks: Toward an underliquid superamphiphobic surface, Surf. Coatings Technol. (2019), https://doi.org/10.1016/j.surfcoat.2019.02.062.

[20] G. Majano, J. Pérez-Ramírez, Scalable room-temperature conversion of copper(II) hydroxide into HKUST-1 (Cu3(btc)2), Adv. Mater. (2013), https://doi.org/10.1002/adma.201203664.

[21] D. Yan, J. Zhang, F. Yuan, X. Zhang, Visualized detection of water by modified metal organic framework-199 and its portable test paper with reversible color change, Spectrochim. Acta - Part A Mol. Biomol. Spectrosc. (2024), https://doi.org/10.1016/j.saa.2024.124151.

[22] P. Liu, K. Cai, K. Wang, T. Zhao, D.J. Tao, Highly defective HKUST-1 with excellent stability and SO2 uptake: the hydrophobic armor effect of functionalized ionic liquids, Green Energy Environ. (2024), https://doi.org/10.1016/j.gee.2023.10.003.

[23] D. Liu, P. Jiang, X. Li, J. Liu, L. Zhou, X. Wang, F. Zhou, 3D printing of metal-organic frameworks decorated hierarchical porous ceramics for high-efficiency catalytic degradation, Chem. Eng. J. (2020), https://doi.org/10.1016/j.cej.2020.125392.

[24] M. del Rio, M. Villar, S. Quesada, G. Turnes Palomino, L. Ferrer, C. Palomino Cabello, Silver-functionalized UiO-66 metal-organic framework-coated 3D printed device for the removal of radioactive iodine from wastewaters, Appl. Mater. Today (2021), https://doi.org/10.1016/j.apmt.2021.101130.

[25] Y.N. Reddy, A. De, S. Paul, A.K. Pujari, J. Bhaumik, In situ nanoarchitectonics of a MOF hydrogel: a self-adhesive and pH-responsive smart platform for phototherapeutic delivery, Biomacromolecules (2023), https://doi.org/10.1021/acs.biomac.2c01489.

[26] A.F. Kateshali, F. Moghzi, J. Soleimannejad, J. Janczak, In situ growth of luminescent d-f MOF nanostructures on bacterial cellulose as an accessible kit for early jaundice diagnosis, Sci. Rep. (2025), https://doi.org/10.1038/s41598-025-94147-2.

[27] H. Molavi, K. Mirzaei, M. Barjasteh, S.Y. Rahnamaee, S. Saeedi, A. Hassanpouryouzband, M. Rezakazemi, 3D-printed MOF monoliths: fabrication strategies and environmental applications, Nano-Micro Lett. (2024), https://doi.org/10.1007/s40820-024-01487-1.

[28] S. Lawson, A.A. Alwakwak, A.A. Rownaghi, F. Rezaei, Gel-print-grow: a new way of 3D Printing metal-organic frameworks, ACS Appl. Mater. Interfaces (2020), https://doi.org/10.1021/acsami.0c18720.

[29] R. Bhosale, S. Gupta, B. Kandasubramanian, Advances in metal-organic frameworks for use in 3D printing techniques, ChemistrySelect (2025), https://doi.org/10.1002/slct.202404898.

[30] D. Pianca, M. Carboni, D. Meyer, 3D-printing of porous materials: application to metal-organic frameworks, Mater. Lett.: X (2022), https://doi.org/10.1016/j.mlblux.2022.100121.

[31] B. Chen, R. Davies, H. Chang, Y. Xia, Y. Zhu, O. Ghita, In-situ synthesis of metal organic frameworks (MOFs)-PA12 powders and their laser sintering into hierarchical porous lattice structures, Addit. Manuf. (2021), https://doi.org/10.1016/j.addma.2020.101774.

[32] D. Liu, P. Jiang, X. Wang, W. Liu, Additively manufacturing metal-organic frameworks and derivatives: methods, functional objects, and applications, ACS Symp. Ser. (2021), https://doi.org/10.1021/bk-2021-1393.ch002.

[33] O. Gohar, I. Nisa, M. Saleem, H. Zhou, M.Z. Khan, M.M. Baig, M. Ali, J.H. Koh, A. Riaz, Y. Zhang, H. Pang, 3D printing of metal-organic frameworks for electrochemical energy storage devices, Coord. Chem. Rev. (2026), https://doi.org/10.1016/j.ccr.2025.217353.

[34] W.Y. Lieu, D. Fang, K.J. Tay, X.L. Li, W.C. Chu, Y.S. Ang, D.S. Li, L.K. Ang, Y. Wang, H.Y. Yang, Progress on 3D-printed metal-organic frameworks with hierarchical

structures, Adv. Mater. Technol. (2022), https://doi.org/10.1002/admt.202200023.
[35] J. Dhainaut, M. Bonneau, R. Ueoka, K. Kanamori, S. Furukawa, Formulation of metal-organic framework inks for the 3D printing of robust microporous solids toward high-pressure gas storage and separation, ACS Appl. Mater. Interfaces (2020), https://doi.org/10.1021/acsami.9b22257.
[36] S.A. Hashemi, A. Ghaffarkhah, A.A. Isari, M. Panahi-Sarmad, F. Jiang, O.J. Rojas, S. Wuttke, M. Dincă, M. Arjmand, Advancing from MOFs and COFs to Functional Macroscopic Porous Constructs, Adv. Mater. (2025), https://doi.org/10.1002/adma.202411617.
[37] A. Bigham, N. Islami, A. Khosravi, A. Zarepour, S. Iravani, A. Zarrabi, MOFs and MOF-based composites as next-generation materials for wound healing and dressings, Small (2024), https://doi.org/10.1002/smll.202311903.
[38] C. Chen, X. Sang, D. Gao, Z. Zhu, W. Wu, Y. Zhao, J.T. Miao, R. Liu, Heterostructured photoinitiator comprising upconversion particles and metal-organic frameworks for enhanced near-infrared photopolymerization: implications for 3D printing, ACS Appl. Polym. Mater. (2024), https://doi.org/10.1021/acsapm.4c02205.
[39] E. Lahtinen, R.L.M. Precker, M. Lahtinen, E. Hey-Hawkins, M. Haukka, Selective laser sintering of metal-organic frameworks: production of highly porous filters by 3D printing onto a polymeric matrix, ChemPlusChem (2019), https://doi.org/10.1002/cplu.201900081.
[40] R. Li, S. Yuan, W. Zhang, H. Zheng, W. Zhu, B. Li, M. Zhou, A. Wing-Keung Law, K. Zhou, 3D printing of mixed matrix films based on metal-organic frameworks and thermoplastic polyamide 12 by selective laser sintering for water applications, ACS Appl. Mater. Interfaces. (2019), https://doi.org/10.1021/acsami.9b11840.
[41] A. Bertero, B. Coppola, J. Schmitt, O. Gimello, P. Trens, P. Palmero, J.M. Tulliani, 3D printed mullite monoliths with triply periodic minimal surface (TPMS) architectures functionalized with HKUST-1 for CO2 capture, Microporous Mesoporous Mater. (2025), https://doi.org/10.1016/j.micromeso.2025.113601.
[42] J. Feng, J. Fu, X. Yao, Y. He, Triply periodic minimal surface (TPMS) porous structures: from multi-scale design, precise additive manufacturing to multidisciplinary applications, Int. J. Extrem. Manuf. (2022), https://doi.org/10.1088/2631-7990/ac5be6.
[43] P. Karimipour-Fard, A.H. Behravesh, H. Jones-Taggart, R. Pop-Iliev, G. Rizvi, Effects of design, porosity and biodegradation on mechanical and morphological properties of additive-manufactured triply periodic minimal surface scaffolds, J. Mech. Behav. Biomed. Mater. (2020), https://doi.org/10.1016/j.jmbbm.2020.104064.
[44] C. Zhou, H. Zhou, X. Qin, S. Gu, M. Zhang, J. Chen, L. Zhai, H. Pang, Bridging MOF properties to 3D printing: a framework for electrochemical energy storage architectures with synergistic porosity-ion dynamics, Chem. Sci. (2025), https://doi.org/10.1039/d5sc06210a.
[45] S. Lawson, X. Li, H. Thakkar, A.A. Rownaghi, F. Rezaei, Recent advances in 3D printing of structured materials for adsorption and catalysis applications, Chem. Rev. (2021), https://doi.org/10.1021/acs.chemrev.1c00060.
[46] M. Li, S.J. Zinkle, Physical and mechanical properties of copper and copper alloys, Compr. Nucl. Mater. (2012), https://doi.org/10.1016/B978-0-08-056033-5.00122-1.
[47] G. Sciacca, M. Sinico, G. Cogo, D. Bigolaro, A. Pepato, J. Esposito, Experimental and numerical characterization of pure copper heat sinks produced by laser powder bed fusion, Mater. Des. (2022), https://doi.org/10.1016/j.matdes.2022.110415.
[48] F. Calignano, A. Bove, M. Pavese, Processing of pure copper by powder bed fusion with infrared laser, Results Eng. 25 (2025) 104497, https://doi.org/10.1016/J.RINENG.2025.104497.
[49] K.J. Kim, Y. Zhang, P.B. Kreider, X. Chong, A.X. Wang, P.R. Ohodnicki, J.P. Baltrus, C.H. Chang, Nucleation and growth of oriented metal-organic framework thin films on thermal SiO2 surface, Thin Solid Films (2018), https://doi.org/10.1016/j.tsf.2018.05.026.
[50] A. Summerfield, I. Cebula, M. Schröder, P.H. Beton, Nucleation and early stages of layer-by-layer growth of metal organic frameworks on surfaces, J. Phys. Chem. C (2015), https://doi.org/10.1021/acs.jpcc.5b07133.
[51] T. Granato, F. Testa, R. Olivo, Catalytic activity of HKUST-1 coated on ceramic foam, Microporous Mesoporous Mater. (2012), https://doi.org/10.1016/j.micromeso.2011.12.055.
[52] W.W. Lestari, M. Adreane, C. Purnawan, H. Fansuri, N. Widiastuti, S.B. Rahardjo, Solvothermal and electrochemical synthetic method of HKUST-1 and its methane storage capacity, IOP Conf. Ser.: Mater. Sci. Eng. (2016), https://doi.org/10.1088/1757-899X/107/1/012030.
[53] A. Umemura, S. Diring, S. Furukawa, H. Uehara, T. Tsuruoka, S. Kitagawa, Morphology design of porous coordination polymer crystals by coordination modulation, J. Am. Chem. Soc. (2011), https://doi.org/10.1021/ja204233q.
[54] Y. Mao, W. Cao, J. Li, Y. Liu, Y. Ying, L. Sun, X. Peng, Enhanced gas separation through well-intergrown MOF membranes: seed morphology and crystal growth effects, J. Mater. Chem. A (2013), https://doi.org/10.1039/c3ta12402a.
[55] Y. Wu, A. Kobayashi, G.J. Halder, V.K. Peterson, K.W. Chapman, N. Lock, P. D. Southon, C.J. Kepert, Negative thermal expansion in the metal-organic framework material Cu 3(1,3,5-benzenetricarboxylate)2, Angew. Chemie - Int. Ed. (2008), https://doi.org/10.1002/anie.200803925.
[56] K. Schlichte, T. Kratzke, S. Kaskel, Improved synthesis, thermal stability and catalytic properties of the metal-organic framework compound Cu3(BTC)2, Microporous Mesoporous Mater. (2004), https://doi.org/10.1016/j.micromeso.2003.12.027.
[57] S. Nikkhah, S. Zendehboudi, N. Rezaei, N.M.C. Saady, A comprehensive review of metal–organic frameworks (MOFs) applications as sorbents and membranes for carbon capture through direct air capture (DAC) technology, Fuel 416 (2026) 137999, https://doi.org/10.1016/J.FUEL.2025.137999.